

Cite this: *Chem. Sci.*, 2022, 13, 4573

All publication charges for this article have been paid for by the Royal Society of Chemistry

An unprecedented fully reduced $\{\text{Mo}^{\text{V}}_{60}\}$ polyoxometalate: from an all-inorganic molecular light-absorber model to improved photoelectronic performance†

Xue-Xin Li,^{‡a} Tuo Ji,^{‡a} Jun-Yang Gao,^{‡a} Wei-Chao Chen,^{ID *a} Ye Yuan,^{ID a} Hao-Yan Sha,^b Roland Faller,^{ID b} Guo-Gang Shan,^{ID a} Kui-Zhan Shao,^a Xin-Long Wang,^{ID *a} and Zhong-Min Su,^{ID a}

Fully reduced polyoxometalates are predicted to give rise to a broad and strong absorption spectrum, suitable energy levels, and unparalleled electronic and optical properties. However, they are not available to date. Here, an unprecedented fully reduced polyoxomolybdate cluster, namely $\text{Na}_8[\text{Mo}^{\text{V}}_{60}\text{O}_{140}(\text{OH})_{28}] \cdot 19\text{H}_2\text{O}$ ($\{\text{Mo}^{\text{V}}_{60}\}$), was successfully designed and obtained under hydrothermal conditions, which is rare and is the largest fully reduced polyoxometalate reported so far. The $\{\text{Mo}^{\text{V}}_{60}\}$ molecule describes one Keggin ($\{\varepsilon\text{-Mo}_{12}\}$) encapsulated in an unprecedented $\{\text{Mo}_{24}\}$ cage, giving rise to a double truncated tetrahedron quasi-nesting architecture, which is further face-capped by another four $\{\text{Mo}_6\}$ tripods. Its crystalline stability in air, solvent tolerance, and photosensitivity were all shown. As a cheap and robust molecular light-absorber model possessing wide light absorption, $\{\text{Mo}^{\text{V}}_{60}\}$ was applied to build a co-sensitized solar cell photoelectronic device along with N719 dyes and the optimal power conversion efficiency was 28% higher than that of single-dye sensitization. These results show that $\{\text{Mo}^{\text{V}}_{60}\}$ polyoxometalate could serve as an ideal model for the design and synthesis of all-inorganic molecular light-absorbers for other light-driven processes in the future.

Received 5th December 2021
Accepted 23rd March 2022

DOI: 10.1039/d1sc06779f

rsc.li/chemical-science

Introduction

Solar energy, as a clean, environmentally friendly and renewable green energy, holds great promise to overcome the energy shortage originating from the consumption of fossil fuels.^{1,2} To efficiently utilize visible and/or solar light, the capture and storage of sunlight serving as energy for driving the formation and transformation of available chemical fuels and electrical energy is an effective strategy through the artificial photosynthesis process and solar cell devices.³ The photosensitizer for capable light harvesting is the core part of such an energy conversion process and extensive efforts have been devoted as a means of developing accessible light-absorber materials.⁴ In general, molecular light-absorber engineering brings greater

adaptability in the fine-tuning of orbital energetics at the molecular level so as to explore the structure–photosensitization relationship accurately and maximize utilization and conversion of solar photon energy.^{4a} To date, some light-absorbers, including phenoxazine-based sensitizers,^{4b} graphitic carbon nitride^{4c} or CdSe quantum dots,^{4d} and traditional Ru-based N719 complexes,^{4e} have been widely investigated. However, most light-absorbers show several disadvantages such as being composed of unstable organic dyes or noble metals and having only narrow visible light absorption, which particularly limit their practical application. Therefore, the explorations of inexpensive and robust molecular light-absorber models with a wide photoabsorption spectrum for optimized solar energy conversion are of great research significance.

Reduced polyoxometalates (POMs), also called heteropoly blues, can be regarded as a rich “blue electron” storage library, which is completely essential for the enhanced photosensitivity of POMs in the light-driven reaction process (Scheme 1).^{5,6} Its advantages as a light-absorber are as follows: (1) it has a broad and strong absorption spectrum involving the visible and near-infrared regions; (2) its energy levels suitable for effective unidirectional electron injections and photosensitizer regenerations can be easily adjusted at the molecular level through the structure, composition, and electric charge; (3) its oxygen-rich

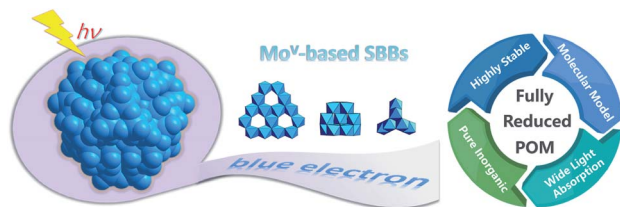
^aKey Laboratory of Polyoxometalate and Reticular Material Chemistry of Ministry of Education, Department of Chemistry, Northeast Normal University, Ren Min Street No. 5268, Changchun, Jilin, 130024 P. R. China. E-mail: chemwc061@nenu.edu.cn; wangxl824@nenu.edu.cn

^bDepartment of Chemical Engineering, University of California, Davis, CA 95616, USA

† Electronic supplementary information (ESI) available: Additional figures, characterization studies and photoelectronic device performance. CCDC 2116971. For ESI and crystallographic data in CIF or other electronic format see DOI: 10.1039/d1sc06779f

‡ These authors have contributed equally.





Scheme 1 Schematic illustration of a fully reduced $\{\text{Mo}^{\text{V}}_{60}\}$ polyoxometalate light-absorber model with its secondary building blocks and features.

surface can be activated and decorated for providing obtainable adsorption and reaction sites; (4) as a cheap and environment-friendly species, it possesses a superior light, electrical, thermal, and redox stability. Thus, unparalleled electronic and optical properties make reduced POMs a popular material for photosensitizers or co-sensitizers with respect to photochemical catalysis and solar cells.^{7,8} To date, there are still few reports on POM-based sensitizer (or co-sensitizer) cell systems. What's more, reduced POMs are mainly obtained *in situ* with the structure hardly air-stable or isolated (*e.g.*, reduced $[\text{P}_2\text{W}_{18}\text{O}_{62}]^{6-}$ for on-demand H_2 generation),⁹ or they are present in mixed valence molybdenum blue stabilized by organic groups suffering from ligand exchange and dissociation (*e.g.*, Keplerate-type $\{\text{Mo}^{\text{V}}_{60}\text{Mo}^{\text{VI}}_{72}\}$ family).¹⁰ In particular, the *d-d* transition of fully reduced POMs, such as inter valence-charge transfer or metal-to-metal charge-transfer, may give rise to a broader absorption spectrum in the visible region for a better light-driven process.¹¹ Accordingly, the discovery and exploration of fully reduced all-inorganic POMs with a well-defined and robust architecture applied as light-absorbers in photoelectronic devices (*e.g.*, dye-sensitized solar cells, DSSCs) will be a significant topic.

Herein, an unprecedented fully reduced POM cluster, namely $\text{Na}_8[\text{Mo}^{\text{V}}_{60}\text{O}_{140}(\text{OH})_{28}] \cdot 19\text{H}_2\text{O}$ ($\text{Mo}^{\text{V}}_{60}$), was successfully obtained and characterized by various physical and chemical technologies, and it remains rare and the largest fully reduced POM so far. Its crystalline stability in air, solvent tolerance, and photosensitivity were all determined. As a cheap and robust molecular light-absorber model featuring wide light absorption, $\{\text{Mo}^{\text{V}}_{60}\}$ was applied to build a co-sensitized solar cell model along with N719 dyes and the optimal efficiency was reached by enhancing sunlight absorption and accelerating electron transport, which is 28% higher than that of single N719 sensitization.

Results and discussion

Structural analysis of $\text{Mo}^{\text{V}}_{60}$

Single-crystal X-ray structure determination revealed that $\text{Mo}^{\text{V}}_{60}$ crystallizes in a tetragonal crystal system with space group $I4_1/acd$ (Table S1†). The $\text{Mo}^{\text{V}}_{60}$ cluster with T_d symmetry is made up of one $\{\text{Mo}_{12}\}$ secondary building block (SBB), four $\{\text{Mo}_6\}$ SBBs and one $\{\text{Mo}_{24}\}$ unit (Fig. 1a and S1 and S2†). The central $\{\text{Mo}_{12}\}$ core exhibits a ε -Keggin structural motif, which can be regarded as an isomer of the most stable α -Keggin and is essentially obtained by rotating 60° along the C_3 axis through all the four $[\text{Mo}_3\text{O}_{13}]^{11-}$ clusters, forming a truncated tetrahedron (Fig. 1e). Structurally, all 12 Mo(v) atoms are arranged in pairs to form six binuclear units (Fig. S3b†) with a $\text{Mo}\cdots\text{Mo}$ distance from 2.5441(19) to 2.6094(16) Å. Such Mo-based ε -Keggin SBBs have been widely used to construct POM-based extended framework materials in the manner of connected nets, with common examples including functional POM-based metal organic frameworks based on zinc-modified $\{\varepsilon\text{-PMo}_{12}\}$ SBBs.¹² Here, the SBB acts as anion template species in the assembly of

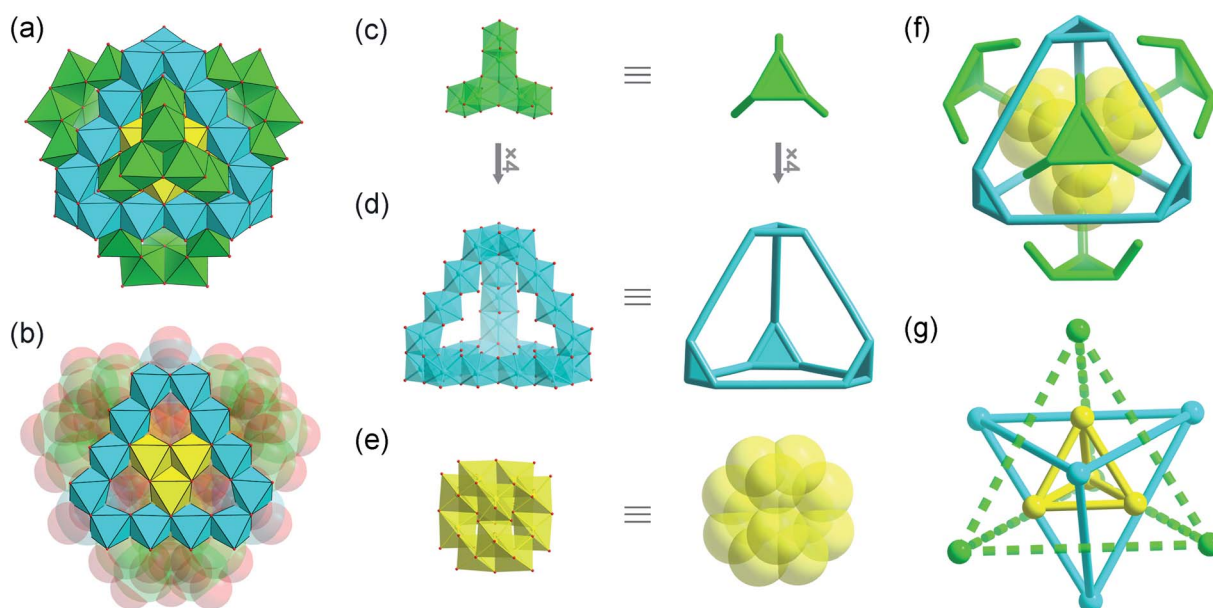


Fig. 1 Polyhedral and ball-and-stick representations of (a) $\text{Mo}^{\text{V}}_{60}$, (b) planar $\{\text{Mo}_{15}\}$, (c) tripod-shaped $\{\text{Mo}_6\}$ (green), (d) truncated tetrahedron $\{\text{Mo}_{24}\}$ (cyan), (e) $\{\varepsilon\text{-Mo}_{12}\}$ (yellow), (f) and (g) the simplified metallic skeleton of $\text{Mo}^{\text{V}}_{60}$.



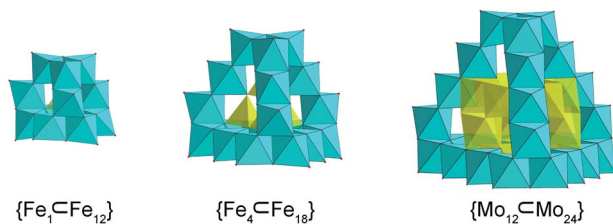


Fig. 2 Polyhedral representations of the truncated tetrahedral cages: (a) $\{\text{Fe}^{\text{III}}_{12}\}$, (b) $\{\text{Fe}^{\text{III}}_{18}\}$ and (c) $\{\text{Mo}^{\text{V}}_{24}\}$. The “trapping” templates are shown in the yellow polyhedra.

$\text{Mo}^{\text{V}}_{60}$. As expected, this template structural evolution may have originated from a “trapping” process in the cage-like $\{\text{Mo}_{24}\}$ host structure. The $\{\text{Mo}_{24}\}$ unit is built by four tripod-shaped $\{\text{Mo}_6\}$ SBBs that are linked to each other through sharing edges, giving rise to a truncated tetrahedral structure (Fig. 1d and S3a†). In this regard, the basic $\{\text{Mo}_6\}$ SBB is composed of three dumbbell-shaped $\{\text{Mo}_2\}$ units by sharing three edges and a common vertex (Fig. 1c) as discovered in the reported Mo-based hollow dodecahedron, whereas the later $\{\text{Mo}_6\}$ SBBs require extra SO_3^{2-} or SO_4^{2-} anion ligands (Fig. S4†).¹³ Remarkably, the appearance of the cage-like $\{\text{Mo}^{\text{V}}_{24}\}$ structure is not a fortuity, whose matrix may be derived from classical molecular iron oxide clusters,¹⁴ e.g. $\{\text{Fe}^{\text{III}}_{17}\}$ ^{14a} and $\{\text{Fe}^{\text{III}}_{34}\}$ ^{14b} (Fig. S5†). The number of Fe or Mo atoms in tetrahedral edges increasing in a regular fashion is responsible for the formation of this truncated tetrahedral cage family, namely $\{\text{Fe}^{\text{III}}_{12}\}$,^{14a} $\{\text{Fe}^{\text{III}}_{18}\}$ ^{14b} and $\{\text{Mo}^{\text{V}}_{24}\}$ (Fig. 2). As a result, the “trapping” templates also undergo contrasting growth (from simple $\{\text{Fe}^{\text{III}}_1\}$ and $\{\text{Fe}^{\text{III}}_4\}$ to bigger $\{\text{Mo}^{\text{V}}_{12}\}$) in their own sizes and complexities. The discoveries of such structural similarities are beneficial to explore the relationships between molecular metal oxide clusters and bulk metal oxides. In addition, each octahedral Fe center in $\{\text{Fe}^{\text{III}}_{12}\}$ and $\{\text{Fe}^{\text{III}}_{18}\}$ needs to be combined with ethoxy or pyridine groups for complete stabilization,^{14b,c} while all the Mo atoms in $\{\text{Mo}_{24}\}$ are not coordinated with any organic ligands. The inner cavity diameter of the purely inorganic $\{\text{Mo}_{24}\}$ cage remains approximately 6.4 Å (Fig. S6†), which is a close fit for the loading of the ϵ -Keggin $\{\text{Mo}_{12}\}$ SBB. This package process occurs in the four edge-sharing $[\text{Mo}_3\text{O}_{10}(\text{OH})_3]^{8-}$ cluster (three single protonated $\mu_2\text{-O}$ atoms proved by bond valence sum (BVS) calculations,¹⁵ Tables S2 and S3†) in the $\{\text{Mo}_{12}\}$ SBB occupying each window of the truncated tetrahedron, respectively, and thus contributes a nested $\{\text{Mo}_{12}\}$ -in- $\{\text{Mo}_{24}\}$ aggregate with a common formula of $\{\text{Mo}_{36}\}$ (Fig. 2). The inner and outer truncated tetrahedra constructed by covalent interactions follow the basic “small vs. large” mode.¹⁶ To the best of our knowledge, such a close packed pattern of nested double truncated tetrahedra has not been seen in POM chemistry (Fig. 1f).

It is worth noting that an unprecedented planar $\{\text{Mo}_{15}\}$ (Fig. 1b) assembly can be identified in $\{\text{Mo}_{36}\}$: 3 central Mo atoms are surrounded by 12 outer Mo atoms belonging to the edges of the hexagonal planar structure. Crucially, such planar species are presented in polyoxomolybdate for the first time. A

similar hexagonal planar structure¹⁷ also appeared in tungsten-containing planar $\{\text{Mn}_6\text{W}_6\}$ (Fig. S7†), and both planar configurations lay the foundation for building POM-based cage-like superclusters. Finally, each planar $\{\text{Mo}_{15}\}$ is further connected by one tripod-shaped $\{\text{Mo}_6\}$ SBB *via* nine $\mu_3\text{-O}$ bridges to form $\text{Mo}^{\text{V}}_{60}$. The $\{\text{Mo}_6\}$ cap possesses four single protonated oxygen atoms (Fig. S8 and Table S2,† 3 $\mu_2\text{-O}$ and 1 $\mu_3\text{-O}$ atoms according to BVS calculations). In general, if each $\{\text{Mo}_3\text{O}_{13}\}$ cluster in $\{\text{Mo}_{12}\}$, $\{\text{Mo}_{24}\}$ and $\{\text{Mo}_6\}$ serves as a vertex, thereby the whole molecular cluster can afford a tri-tetrahedral quasi-nesting structure (Fig. 1g and S9†), which is entirely distinct from the previously described wheel- and spherical-shaped polyoxomolybdate archetypes by Müller *et al.*¹⁸ BVS calculations indicate that overall metal centers are Mo^{V} (Table S4†), which corresponds to the results of the X-ray photoelectron spectroscopy (XPS) analysis (Fig. S10†). Additionally, the generation of unprecedented tripod-shaped $\{\text{Mo}_6\}$ and planar $\{\text{Mo}_{15}\}$ as well as truncated tetrahedral $\{\text{Mo}_{24}\}$ entities brings the $\{\text{Mo}^{\text{V}}_{60}\}$ supercluster. The outer diameter of the whole cluster is approximately *ca.* 15 Å (Fig. S11†), and is the largest fully reduced POM reported so far.

Stability and photochemical characterization of $\text{Mo}^{\text{V}}_{60}$

$\text{Mo}^{\text{V}}_{60}$ retains crystalline stability for at least two weeks when exposed to air and to common organic solvents (e.g. CH_3CN , CH_3OH , and CH_2Cl_2) after soaking for 24 h, as confirmed by powder X-ray diffraction (PXRD) analysis (Fig. 3a). The UV/vis spectrum of $\text{Mo}^{\text{V}}_{60}$ polyoxoanion in solution remains unchanged over the 24 hour monitoring process (Fig. S12†). Moreover, its stability in water was also explored by electrospray ionization mass spectroscopy (ESI-MS), and we found that the whole cluster associated with Na^+ and H^+ ions dominated the solution of redissolved pure $\text{Mo}^{\text{V}}_{60}$ (Fig. S13 and Table S5†). The Ba^{2+} cation exchange experiment of $\text{Mo}^{\text{V}}_{60}$ was conducted.¹⁹ The uniformity

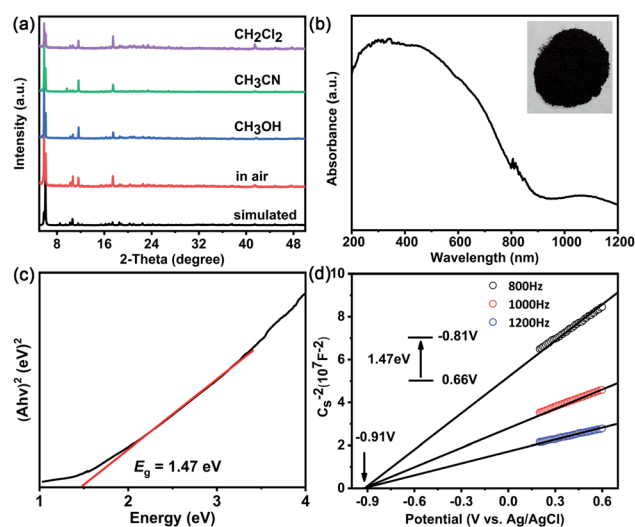


Fig. 3 (a) Simulated and experimental PXRD patterns of $\text{Mo}^{\text{V}}_{60}$ in air or common organic solvents. (b) The UV-vis-NIR absorption spectra of $\text{Mo}^{\text{V}}_{60}$. Inset: solid sample photo of $\text{Mo}^{\text{V}}_{60}$. (c) Tauc plots. Inset: band-gap energy of $\text{Mo}^{\text{V}}_{60}$. (d) Mott-Schottky plots for $\text{Mo}^{\text{V}}_{60}$.

of the IR reliable fingerprint peaks between Na- and Ba-derivatives gives strong evidence that the MoV_{60} cluster is stable (Fig. S14†). Such inherent air-stable features and solvent tolerance are beneficial for better evaluation of its potential photochemical applications. Therefore, solid ultraviolet-visible-near-infrared (UV-vis-NIR) spectroscopy was carried out to assess the photosensitivity of MoV_{60} . As shown in Fig. 3b, it exhibits a wide absorption range including UV, visible and even observable responses in near-infrared regions, which makes it suitable for harvesting more solar light under simulated AM 1.5 illumination. On this basis, the corresponding well-defined optical band-gap energies can be assessed at about 1.47 eV based on its diffuse reflectance spectrum (Fig. 3c). Meanwhile, the relevant conduction band of MoV_{60} was identified and converted to vs. the normal hydrogen electrode (NHE) by Mott-Schottky measurements (Fig. 3d) at frequencies of 800, 1000, and 1200 Hz, which features a higher conduction band and smaller E_g compared to pure TiO_2 (Fig. S15†).²⁰ These characteristics render MoV_{60} a robust all-inorganic molecular semiconductor light-absorber material for TiO_2 -based photovoltaic application.

Morphologies and compositions of $\text{MoV}_{60}/\text{TiO}_2$ photoanodes

The scanning electron microscopy (SEM) image of the $\text{MoV}_{60}/\text{TiO}_2$ composite photoanode displays a homogeneous morphology composed of spherical and granular particles as expected (Fig. 4a). The corresponding energy dispersive spectrometry (EDS) analysis indicates the existence of Ti and Mo (Fig. S16†). TEM was conducted to further explore the morphologies and compositions of $\text{MoV}_{60}/\text{TiO}_2$ composites (Fig. 4b). Compared to the pure TiO_2 sample (Fig. S17†), the average diameter (≈ 25 nm) of the composite in Fig. 4b did not change significantly and its surface was rougher with many tiny particles (Fig. S18†) featuring the approximate size (≈ 2 nm) of MoV_{60} . Such uniformly distributed MoV_{60} granules with little aggregation provide a favorable guarantee for effective photoelectric conversion. Meanwhile, the elemental mapping of the $\text{MoV}_{60}/\text{TiO}_2$ composite clearly proves the homogeneous distribution of MoV_{60} and TiO_2 in the composite (Fig. 4c). XRD was performed to track the changes in the TiO_2 phase in the $\text{MoV}_{60}/\text{TiO}_2$ composite. Fig. 4d illustrates that the characteristic peaks of the composites are in agreement with those of anatase TiO_2

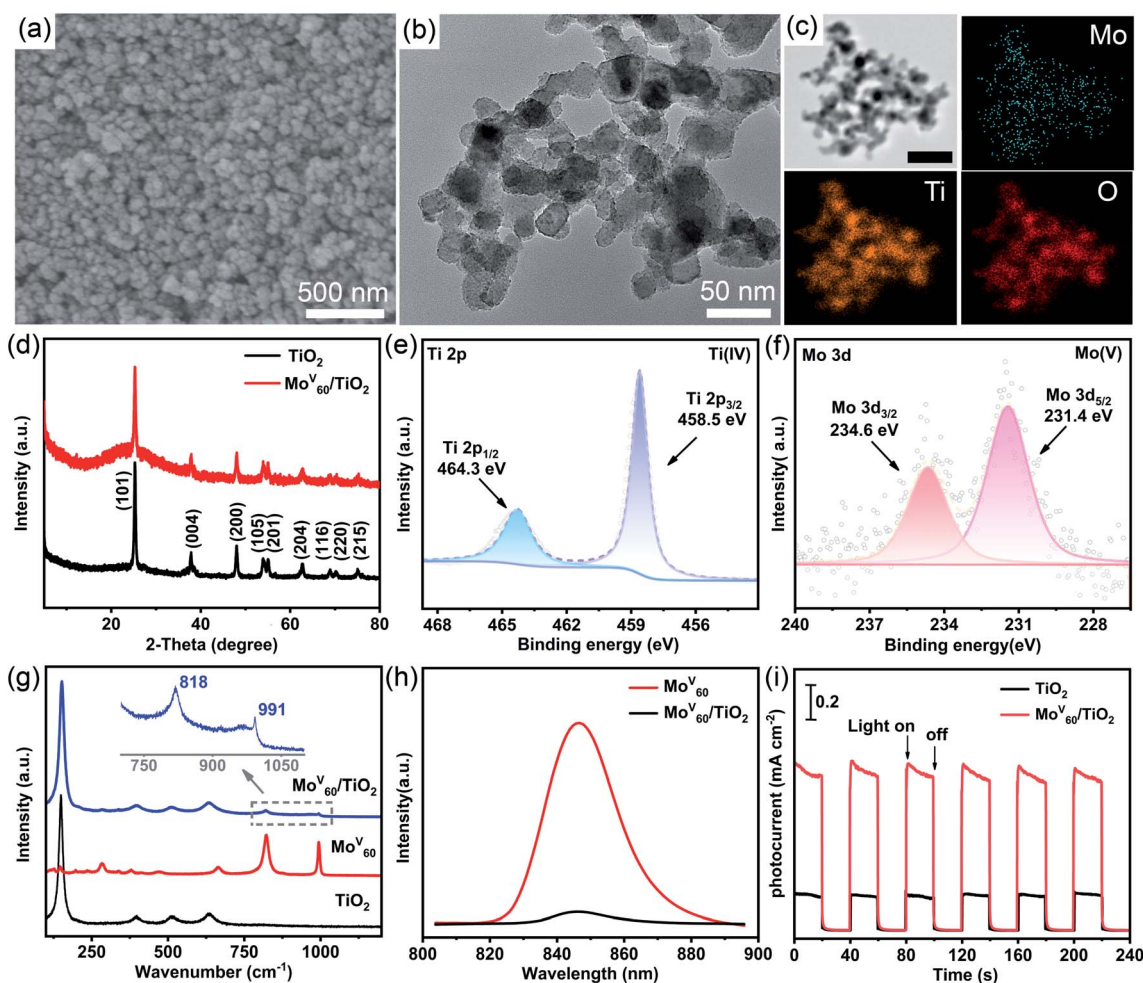


Fig. 4 (a) SEM and (b) TEM images of the $\text{MoV}_{60}/\text{TiO}_2$ composite photoanode with relevant (c) elemental mapping analyses (scale bar: 100 nm). (d) PXRD patterns of calcined TiO_2 and $\text{MoV}_{60}/\text{TiO}_2$ composites. (e) and (f) High resolution XPS spectra of Ti 2p and Mo 3d in a $\text{MoV}_{60}/\text{TiO}_2$ composite. (g) Raman spectra of calcined TiO_2 , MoV_{60} and $\text{MoV}_{60}/\text{TiO}_2$ composites. (h) The emission spectra of MoV_{60} and $\text{MoV}_{60}/\text{TiO}_2$ composites. (i) Photocurrent responses with on-off light illumination of TiO_2 and $\text{MoV}_{60}/\text{TiO}_2$ composites.



(JCPDS no. 21-1272), which shows that the crystal phase of TiO_2 undergoes no changes after the introduction of $\text{Mo}^{\text{V}}_{60}$. The XPS of the $\text{Mo}^{\text{V}}_{60}/\text{TiO}_2$ composite (Fig. 4e and f) was used to study the surface composition and the oxidation states of Mo and Ti elements. The XPS peaks of Ti in the $\text{Mo}^{\text{V}}_{60}/\text{TiO}_2$ composite are centered at 458.5 and 464.3 eV, respectively, corresponding to the binding energy of Ti 2p_{3/2} and Ti 2p_{1/2} as reported in the literature.⁸ As for Mo atoms, two peaks at 231.4 and 234.6 eV ascribed to Mo^{5+} 3d_{5/2} and 3d_{3/2}, respectively, far from the $\text{Mo}(\text{iv})$ or $\text{Mo}(\text{vi})$ binding energies (Table S6†), clearly testify the persistent $\text{Mo}(\text{v})$ oxidation state during the $\text{Mo}^{\text{V}}_{60}$ composite process.^{12c,21} The Raman spectrum (Fig. 4g) of $\text{Mo}^{\text{V}}_{60}$ featuring two relatively strong peaks at 991 and 818 cm^{-1} could be assigned to the vibrations of terminal $\text{Mo}=\text{O}$ bands and $\text{Mo}-\text{O}-\text{Mo}$ bridges, respectively.²² The peaks located at 147, 396, 511, and 635 cm^{-1} of calcined TiO_2 belong to the typical anatase phase²³ as proved by the XRD results. As expected, both characteristic peaks could be well identified in the $\text{Mo}^{\text{V}}_{60}/\text{TiO}_2$ composite, which further clarified the integrity of TiO_2 and $\text{Mo}^{\text{V}}_{60}$ in the composite photoanode. Photoluminescence (PL) was conducted to explore the charge transfer process between $\text{Mo}^{\text{V}}_{60}$ and TiO_2 . Fig. 4h shows that the fluorescence emission band of $\text{Mo}^{\text{V}}_{60}$ is around 850 nm upon excitation at 553 nm and it could be efficiently quenched by the addition of TiO_2 . Such a quenching phenomenon proves that the photo-induced electron transfer process could be established from $\text{Mo}^{\text{V}}_{60}$ to TiO_2 because of the higher conduction band of the former. Thus we can see that the charge recombination of $\text{Mo}^{\text{V}}_{60}$ has been availablely suppressed.²⁴ What's more, the photocurrent response remains a useful test to further evaluate this electron-transfer phenomenon (Fig. 4i). The photocurrent changes along with the irradiation being switched on and off have been recorded under simulated solar illumination. The photocurrent response intensity of $\text{Mo}^{\text{V}}_{60}/\text{TiO}_2$ is nearly five times higher than that of pure TiO_2 , which may be derived from the generated photocurrent by the introduction of $\text{Mo}^{\text{V}}_{60}$ upon excitation with visible light. This result shows that $\text{Mo}^{\text{V}}_{60}$ could increase the photoresponse of TiO_2 from the UV to visible light region. In total, all related results further indicate the successful preparation of compositions of $\text{Mo}^{\text{V}}_{60}/\text{TiO}_2$ photoanodes.

Performance of $\{\text{Mo}^{\text{V}}_{60}\}/\text{N719}$ co-sensitized DSSCs

In previous studies, the classical DSSCs (Fig. 5a) were assembled with the sensitized photoanodes, the electrolyte containing the redox pairs (I^-/I_3^-) and a Pt counter electrode.⁸ So a series of $\text{Mo}^{\text{V}}_{60}/\text{N719}$ co-sensitized photoanodes with different amounts of $\{\text{Mo}^{\text{V}}_{60}\}$ were fabricated and the performance of these co-sensitized electrodes in DSSCs under simulated AM 1.5 illumination (100 mW cm^{-2}) and in the dark was investigated. The performances of the DSSCs based on $\text{Mo}^{\text{V}}_{60}/\text{N719}$ co-sensitized photoanodes were evidently enhanced compared to single N719 sensitized cells (Fig. S19 and S20†). What's more, the amount of the co-sensitizer had profound effects on the performances and the cells with 5% $\{\text{Mo}^{\text{V}}_{60}\}$ yield optimal results. The photocurrent-voltage ($J-V$) results in Fig. 5b show that the circuit current density (J_{sc}) was improved from 13.36 mA cm^{-2} to 15.94 mA

cm^{-2} due to the existence of the 5% $\text{Mo}^{\text{V}}_{60}$ co-sensitizer. The increase in the J_{sc} can be ascribed to more efficient electronic injection and collection as well as smoother transfer.²⁵ More specifically, the conduction band of $\text{Mo}^{\text{V}}_{60}$ (-0.81 V vs. NHE) is between the conduction band of TiO_2 (-0.5 V vs. NHE) and the excited state of N719 dye (-0.98 V vs. NHE), and the existence of $\text{Mo}^{\text{V}}_{60}$ facilitates charge transfer from N719 to TiO_2 and then promotes electronic injection capacity (Fig. 5a). Simultaneously, the smaller band gap and considerable visible absorption spectrum of $\text{Mo}^{\text{V}}_{60}$ provide the co-sensitized solar cell with more sunlight absorption for enhancing the visible photocurrent response. The improvement of the open circuit voltage (V_{oc}) from 682 to 734 mV could be attributed to suppressed carrier recombination that proceeded at the interface of dye/ TiO_2 /electrolyte, which could also be verified by the lower dark current in $\text{Mo}^{\text{V}}_{60}/\text{N719}$ co-sensitized DSSCs (Fig. 5b). Finally, the overall power conversion efficiency (η) of the co-sensitized cell (6.63%) shows an improvement of up to 28% compared with that of a single N719 sensitized cell (5.18%) (Table S7†). The incident photon conversion efficiency (IPCE) was carried out to better study the photocurrent response to incident light so as to evaluate the performance of the DSSCs at diverse wavelengths of light.²⁶ As expected, $\text{Mo}^{\text{V}}_{60}/\text{N719}$ co-sensitized DSSCs reveal higher IPCE than the single N719 sensitized cell (Fig. 5c), which may ascribed to both more sunlight capture and faster electron transport in the photoanode after the introduction of the $\text{Mo}^{\text{V}}_{60}$ molecular light-absorber model.

To further understand the intrinsic mechanism of sensitized DSSCs, we developed an electrochemical impedance spectroscopy (EIS) experiment to uncover the internal resistances. The Nyquist curves of the DSSCs based on the $\text{Mo}^{\text{V}}_{60}/\text{TiO}_2/\text{N719}$ photoanode and $\text{TiO}_2/\text{N719}$ photoanode are well depicted in Fig. S21a.† The small semicircles at high frequency belong to the charge-transfer resistance at the interface of the counter electrode-electrolyte (R_{pt}), while another semicircle represents the charge-transfer resistance at the TiO_2 -dye-electrolyte interface (R_{ct}) involving charge transport or recombination.²⁷ Obviously, the $\text{Mo}^{\text{V}}_{60}/\text{N719}$ sample possesses a higher R_{ct} , which proves that a smoother and efficient electron transfer process was built through the charge recombination behavior reduced by the $\text{Mo}^{\text{V}}_{60}$ molecular co-sensitizer. Furthermore, the Bode phase plots of the EIS results are presented in Fig. S21b.† The electron lifetime (τ_e) in both photoanodes could be calculated by using the following formula: $\tau_e = \omega_{\text{min}}^{-1} = (2\pi f_{\text{max}})^{-1}$, in which the f_{max} value remains the characteristic frequency peak at the top of the intermediate frequency arc. In this way, the lower frequency in the $\text{Mo}^{\text{V}}_{60}/\text{N719}$ co-sensitized photoanode has a longer τ_e . This is in line with the dark current analyses, demonstrating the effective suppressant during the carrier recombination.

In the meantime, the open-circuit voltage decay (OCVD) is utilized to further verify the aforementioned results by monitoring the fading trend of V_{oc} after switching off the illumination within a fixed time.²⁸ As depicted in Fig. 5d, we can conclude that a slower photovoltage decay rate of the DSSCs based on the $\text{Mo}^{\text{V}}_{60}/\text{N719}$ sample is clearly presented, which demonstrates that the involved electron recombination kinetics



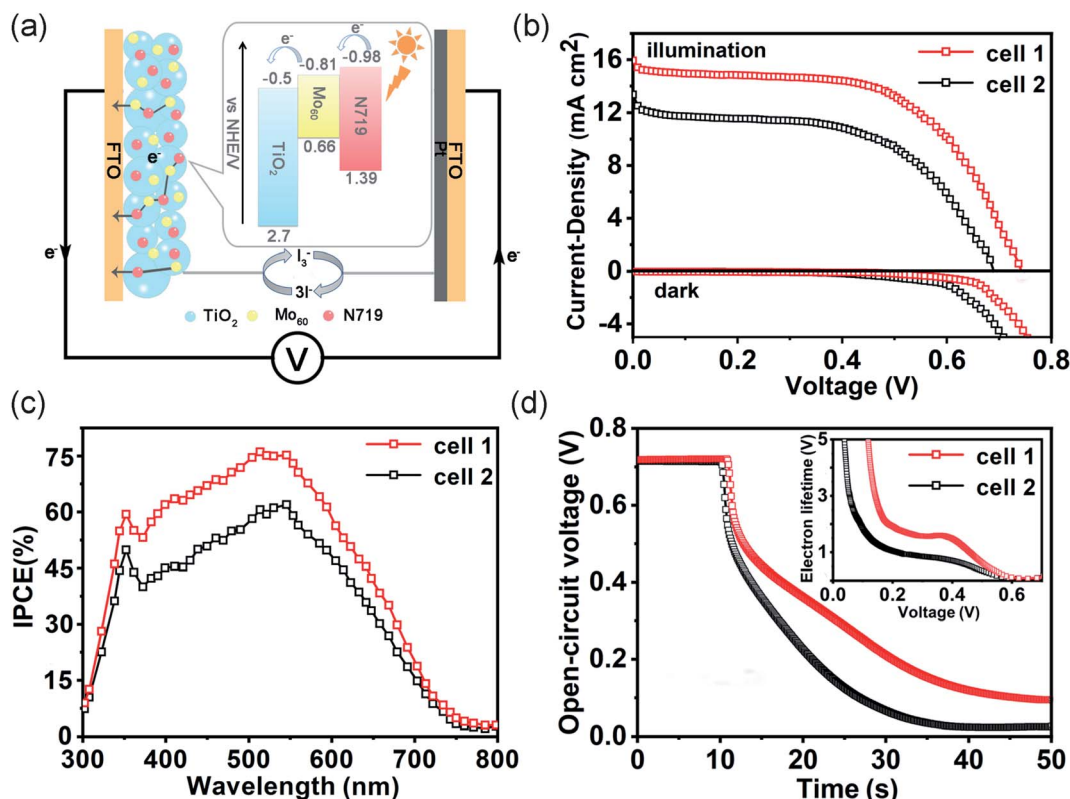


Fig. 5 (a) Energy levels of TiO₂, Mo^V₆₀ and N719 in DSSCs. (b) *J*-*V* curves of DSSCs based on single N719 and Mo^V₆₀/N719 sensitization. (c) IPCE for DSSCs with single N719 and Mo^V₆₀/N719 sensitization. (d) OCVD spectra of DSSCs with N719 and Mo^V₆₀/N719 sensitization. Inset illustration shows their relevant electron lifetime (cell 1: Mo^V₆₀/N719 co-sensitization, cell 2: single N719 sensitization).

have been suppressed effectively. Further, the electron lifetime could also be calculated by using the formula $\tau_e = (kT/e)(dV/dt)^{-1}$ based on the OCVD curves. It is evident that the Mo^V₆₀/N719 sample shows a longer electron lifetime than the pure N719 sample, and such a trend is in accordance with EIS analysis. Thus, the introduction of the Mo^V₆₀ molecular co-sensitized light-absorber model is conducive to the transmission of photogenerated electrons along with an enhancement in the DSSC efficiency.

Experimental

All commercially available reagents, including H₂MoO₄, HCl, Na₂S₂O₄, and ethanol were purchased from Aldrich and used without further purification. Detailed characterization methods including the structural, stability and photochemical analysis of Mo^V₆₀, and morphologies and compositions of Mo^V₆₀/TiO₂ photoanodes as well as related co-sensitizer performance in photoelectronic devices have been fully presented in the ESI.†

Synthesis of Mo^V₆₀

H₂MoO₄ (0.088 g, 0.5 mmol) and Na₂S₂O₄ (0.174 g, 1 mmol) were dissolved in 10 ml of deionized water, respectively. The mixture was added to 500 μl 3.0 M HCl (aq.) and stirred for about 45 min until the solution colour was deep blue. Subsequently, the Mo-containing aqueous solution was transferred to a 25 Teflon-lined stainless-steel container, which was heated to

170 °C and kept for 72 hours, then slowly cooled to room temperature. The solution was kept in an open 15 ml beaker for about one week. The dark red crystals were collected and washed with ethanol. (13 mg, yield 18% based on Mo). IR (cm⁻¹): 1620 (s), 1402 (s), 963 (s), 916 (w), 824 (w), 775 (w), 741 (s). Elemental analysis% calcd (found): Mo 64.0 (63.9).

Preparation of the Mo^V₆₀/TiO₂ composite photoanode

The sintering process of TiO₂ powder (450 °C, 30 min) was necessary before using. The film electrodes based on TiO₂ paste were obtained through mixing pre-treated TiO₂ with different mass percentages (0%, 3%, 5% and 7%) of Mo^V₆₀. The FTO glass plate, as the substrate of the film electrode, was treated with 40 mM TiCl₄ aqueous solution (70 °C, 30 min) and washed with water and ethanol, respectively. Then, the as-synthesized TiO₂ paste was coated in one layer onto the FTO glass plates *via* screen-printing technology (120 °C, 5 min) giving rise to the film electrodes, which were calcined (300 °C, 30 min) after coating four-layered paste onto each FTO glass. Finally, the obtainable sintered film electrodes were post-treated in 40 mM TiCl₄ solution (70 °C, 30 min) and calcined again (300 °C, 30 min).

Solar cell fabrication

The prepared TiO₂ film electrodes were soaked in anhydrous C₂H₅OH solution containing 0.2 mM N719 for 24 h. The redundant dyes were thoroughly washed with anhydrous



C₂H₅OH and dried under a N₂ atmosphere. The counter electrode was a classical platinum plate. A drop of electrolyte solution based on 0.1 M LiI, 0.05 M I₂, and 0.6 M 1,2-dimethyl-3-propylimidazolium iodide as well as 0.5 M 4-*tert*-butyl-pyridine in 3-methoxypropionitrile was injected between the co-sensitized TiO₂ film and platinum electrodes to complete photo-electronic device fabrication.

Conclusions

In summary, we designed and synthesized a brand-new polyoxomolybdate featuring double truncated tetrahedron quasi-nesting architecture face-capped by four {Mo₆} tripods, in which planar {Mo₁₅} and truncated tetrahedron {Mo₂₄} SBBs have never been seen in POMs. As far as we know, Mo^V₆₀ is the largest fully reduced POM with a definite crystal structure and great stability either in air or common organic solvents. Its photosensitive properties were systematically characterized and it possesses a smaller band gap and higher conduction band than TiO₂. As a cheap and robust molecular light-absorber model featuring wide light absorption, Mo^V₆₀ was employed to assemble a co-sensitized solar cell model along with N719 dyes and the optimal efficiency was reached by enhancing sunlight absorption and accelerating electron transport, which is 28% higher than that of single N719 sensitization. These results show that Mo^V₆₀ could serve as a potential sensitizer candidate for other light-driven reactions. This work may provide some new enlightenment for the design and synthesis of all-inorganic POM-based photosensitizers.

Data availability

The datasets supporting this article have been uploaded as part of this manuscript and its corresponding ESI.† Crystallographic data can be obtained from the CCDC.

Author contributions

W. Chen and X. Wang designed the study and supervised the project. X. Li, T. Ji, and J. Gao performed the experiments. All the authors discussed the results and co-wrote the manuscript.

Conflicts of interest

There are no conflicts to declare.

Acknowledgements

This work was financially supported by the NSFC of China (no. 21801038, 21671034 and 21771035), Natural Science Foundation of Jilin Province – Free Exploration General Project, and the Science and Technology Research Foundation of Jilin Educational Committee (JJKH20221158KJ).

Notes and references

- 1 A. Rode, T. Carleton, M. Delgado, M. Greenstone, T. Houser, S. Hsiang, A. Hultgren, A. Jina, R. E. Kopp, K. E. McCusker, I. Nath, J. Rising and J. Yuan, *Nature*, 2021, **598**, 308–314.
- 2 N. S. Lewis, *Science*, 2016, **351**, 353–362.
- 3 J. H. Kim, D. Hansora, P. Sharma, J. Jang and J. S. Lee, *Chem. Soc. Rev.*, 2019, **48**, 1908–1971.
- 4 (a) H. Zhang, H. Liu, Z. Tian, D. Lu, Y. Yu, S. Cestellos-Blanco, K. K. Sakimoto and P. Yang, *Nat. Nanotechnol.*, 2018, **13**, 900–905; (b) H. Rao, L. C. Schmidt, J. Bonin and M. Robert, *Nature*, 2017, **548**, 74–77; (c) X. Wang, K. Maeda, A. Thomas, K. Takanebe, G. Xin, J. M. Carlsson, K. Domen and M. Antonietti, *Nat. Mater.*, 2009, **8**, 76–80; (d) H. Lv, T. P. A. Ruberu, V. E. Fleischauer, W. W. Brennessel, M. L. Neidig and R. Eisenberg, *J. Am. Chem. Soc.*, 2016, **138**, 11654–11663; (e) B. O'Regan and M. Grätzel, *Nature*, 1991, **353**, 737–740.
- 5 S.-S. Wang and G.-Y. Yang, *Chem. Rev.*, 2015, **115**, 4893–4962.
- 6 Y. Nishimoto, D. Yokogawa, H. Yoshikawa, K. Awaga and S. Irie, *J. Am. Chem. Soc.*, 2014, **136**, 9042–9052.
- 7 J. Li, W. Chen, L. Chen, X. Zheng, G. Zhu and E. Wang, *Adv. Opt. Mater.*, 2018, **6**, 1800225–1800237.
- 8 L. Chen, W.-L. Chen, X.-L. Wang, Y.-G. Li, Z.-M. Su and E.-B. Wang, *Chem. Soc. Rev.*, 2019, **48**, 260–284.
- 9 J.-J. Chen, M. D. Symes and L. Cronin, *Nat. Chem.*, 2018, **10**, 1042–1047.
- 10 R. W. Pow, W. Xuan, D.-L. Long, N. L. Bell and L. Cronin, *Chem. Sci.*, 2020, **11**, 2388–2393.
- 11 M. Vasilopoulou, A. M. Douvas, L. C. Palilis, S. Kennou and P. Argitis, *J. Am. Chem. Soc.*, 2015, **137**, 6844–6856.
- 12 (a) L. M. Rodriguez-Albelo, A. R. Ruiz-Salvador, A. Sampieri, D. W. Lewis, A. Gómez, B. Nohra, P. Mialane, J. Marrot, F. Sécheresse, C. Mellot-Draznieks, R. N. Biboum, B. Keita, L. Nadj and A. Dolbecq, *J. Am. Chem. Soc.*, 2009, **131**, 16078–16087; (b) Y.-R. Wang, Q. Huang, C.-T. He, Y. Chen, J. Liu, F.-C. Shen and Y.-Q. Lan, *Nat. Commun.*, 2018, **9**, 4466; (c) H. Zhang, W. Liu, A. Li, D. Zhang, X. Li, F. Zhai, L. Chen, L. Chen, Y. Wang and S. Wang, *Angew. Chem., Int. Ed.*, 2019, **58**, 16110–16114.
- 13 J. Lin, N. Li, S. Yang, M. Jia, J. Liu, X.-M. Li, L. An, Q. Tian, L.-Z. Dong and Y.-Q. Lan, *J. Am. Chem. Soc.*, 2020, **142**, 13982–13988.
- 14 (a) G. W. Powell, H. N. Lancashire, E. K. Brechin, D. Coffison, S. L. Heath, T. Mallah and W. Wernsdorfer, *Angew. Chem., Int. Ed.*, 2004, **43**, 5772–5775; (b) A. E. Dearle, D. J. Cutler, H. W. L. Fraser, S. Sanz, E. Lee, S. Dey, I. F. Diaz-Ortega, G. S. Nichol, H. Nojiri, M. Evangelisti, G. Rajaraman, J. Schnack, L. Cronin and E. K. Brechin, *Angew. Chem., Int. Ed.*, 2019, **58**, 16903–16906; (c) O. Nachtigall, M. Kusserow, R. Clérac, W. Wernsdorfer, M. Menzel, F. Renz, J. Mrozinski and J. Spandl, *Angew. Chem., Int. Ed.*, 2015, **54**, 10361–10364; (d) A. Bino, M. Ardon, D. Lee, B. Spingler and S. J. Lippard, *J. Am. Chem. Soc.*, 2002, **124**, 4578–4579.
- 15 I. D. Brown and D. Altermatt, *Acta Crystallogr., Sect. B: Struct. Sci.*, 1985, **41**, 244–247.



- 16 K. Byrne, M. Zubair, N. Zhu, X.-P. Zhou, D. S. Fox, H. Zhang, B. Twamley, M. J. Lennox, T. Düren and W. Schmitt, *Nat. Commun.*, 2017, **8**, 15268–15277.
- 17 C. Zhang, M. Zhang, H. Shi, Q. Zeng, D. Zhang, Y. Zhao, Y. Wang, P. Ma, J. Wang and J. Niu, *Chem. Commun.*, 2018, **54**, 5458–5461.
- 18 A. Müller and P. Gouzerh, *Chem. Soc. Rev.*, 2012, **41**, 7431–7463.
- 19 M. Blasco-Ahicart, J. Soriano-López, J. J. Carbó, J. M. Poblet and J. R. Galan-Mascaros, *Nat. Chem.*, 2018, **10**, 24–30.
- 20 J. Du, Y. Ma, X. Xin, H. Na, Y. Zhao, H. Tan, Z. Han, Y. Li and Z. Kang, *Chem. Eng. J.*, 2020, **398**, 125518–125555.
- 21 Y.-Q. Wei, C. Sun, Q.-S. Chen, M.-S. Wang and G.-C. Guo, *Chem. Commun.*, 2018, **54**, 14077–14080.
- 22 C. Christian Schäffer, A. Merca, H. Bögge, A. M. Todea, M. L. Kistler, T. Liu, R. Thouvenot, P. Gouzerh and A. Müller, *Angew. Chem., Int. Ed.*, 2009, **48**, 149–153.
- 23 F. Tian, Y. Zhang, J. Zhang and C. Pan, *J. Phys. Chem. C*, 2012, **116**, 7515–7519.
- 24 W. Wang, J. Zhang, K. Lin, Y. Dong, J. Wang, B. Hu, J. Li, Z. Shi, Y. Hu, W. Cao, D. Xia, R. Fan and Y. Yang, *Adv. Funct. Mater.*, 2021, 2105884–2105895.
- 25 J. M. Cole, G. Pepe, O. K. A. Bahri and C. B. Cooper, *Chem. Rev.*, 2019, **119**, 7279–7327.
- 26 K. Zeng, Y. Chen, W. Zhu, H. Tian and Y. Xie, *J. Am. Chem. Soc.*, 2020, **142**, 5154–5161.
- 27 F. Bella, S. Galliano, M. Falco, G. Viscardi, C. Barolo, M. Grätzel and C. Gerbaldi, *Chem. Sci.*, 2016, **7**, 4880–4890.
- 28 J. Bisquert, A. Zaban, M. Greenshtein and I. Mora-Seró, *J. Am. Chem. Soc.*, 2004, **126**, 13550–13559.

